ACS OMEGA

Open Access
This article is licensed under CC-BY-NC-ND 4.0

http://pubs.acs.org/journal/acsodf
Article

Facile Sol–Gel Synthesis of C, N Codoped-TiO_2 for Efficient Degradation of Palm Oil Mill Effluent

Benjamin Tze-Wei Tan, Nor Ashikin Mohd. Rashid, Nurul Hidayah Mohamad Idris, Wee Long Wun, and Hooi Ling Lee*

Cite This: *ACS Omega* 2025, 10, 2858–2870
Read Online

ACCESS | Metrics & More | Article Recommendations | Supporting Information

ABSTRACT: Wastewater treatment has been regarded as an effective solution in lowering the potential environmental hazards caused by palm oil mill effluent (POME). To ensure the efficient remediation of POME, the implementation of a promising strategy is necessary to overcome the limitations of conventional water treatment methods for the treatment of this pollutant. In this study, the synthesis of carbon, nitrogen codoped titanium dioxide nanoparticles (C, N-TiO_2 NPs) was successfully performed by a sol–gel approach for the treatment of POME as a model pollutant under solar light irradiation. The synthesized C, N-TiO_2 NPs displayed unique characteristics including an anatase phase with an average crystallite size of 11.35 nm and irregular spherical structures. Additionally, C, N-TiO_2 possessed a lower band gap energy of 2.95 eV than 3.2 V of bulk anatase TiO_2 and slower electron–hole (e^--h^+) pair recombination rate as evidenced by photoluminescence (PL) studies. The adsorption isotherm study of POME was most compatible with the Langmuir isotherm model, and the POME degradation kinetics proceeded according to first-order kinetics. Accordingly, the photocatalytic degradation of POME displayed a maximum degradation efficiency of 100% under the optimum condition of pH 7 in the presence of 0.12 g of the C, N-TiO_2 photocatalyst within 150 min. The scavenging study showed that the superoxide radical ($\bullet O_2^-$) was the primary active species in the POME photodegradation. Finally, the reusability analysis confirmed that the C, N-TiO_2 NPs could be reused for a maximum of five cycles, making them promising photocatalysts for wastewater treatment.

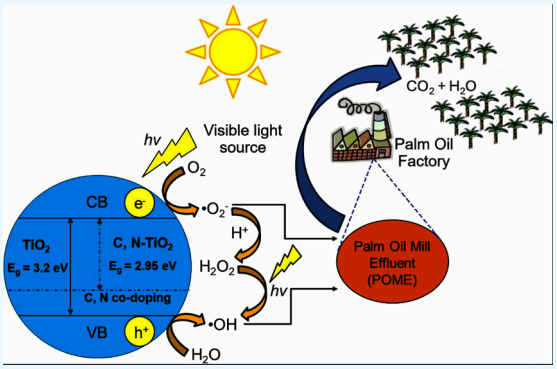

1. INTRODUCTION

Water contamination denotes the existence of physical, chemical, and biological elements that diminish the suitability of a body of water for various purposes.[1] The various sources of water pollution include industrial operations, natural events, agricultural activities, and human actions, involving various types of pollutants, such as microplastics, dyes, antibiotics, and POME. Among these pollutants, considerable attention has been given to POME in recent years due to its long-term existence in wastewater.

POME is a thick, brownish wastewater usually eliminated between 80 and 90 °C and pH 4 and 5. This pollutant is often perceived as a nontoxic liquid waste due to the absence of chemicals being used in oil extraction.[2] The discharge of POME into the environment has emerged as the primary pollutant associated with palm oil mills, which significantly impacts water quality. Consequently, this water cannot be released directly into the environment without the appropriate treatment. Therefore, the ponding system has emerged as a conventional method for the treatment of POME and remains widely utilized in Malaysia due to the extensive land availability and consistently warm climate, thus enhancing the effectiveness of POME removal.[3] Furthermore, it has been observed that POME contains high levels of biochemical and chemical oxygen demands (BOD and COD) as well as acidic pH due to the presence of complex organic acids.[4] Consequently, the rising demand for BOD and COD results in poor water quality.[5]

Wastewater treatment has been proven to be an effective solution in lowering the potential environmental damage that POME might have caused. Several common conventional processes employed in wastewater treatment facilities for the treatment of POME include coagulation/flocculation, precipitation, biodegradation, filtration, and adsorption utilizing activated carbon.[6] Nevertheless, these treatment techniques often result in incomplete remediation of POME as their procedures require extensive systems, infrastructure, and

Received: September 26, 2024
Revised: December 27, 2024
Accepted: January 3, 2025
Published: January 11, 2025

ACS Publications
© 2025 The Authors. Published by American Chemical Society

https://doi.org/10.1021/acsomega.4c08813
ACS Omega 2025, 10, 2858–2870

technical expertise and are chemically and operationally demanding, thus making them laborious, inefficient, time-consuming, and costly.[7]

Given the challenges posed by POME, such as its biodegradable yet land-intensive and odor-emitting nature, palm oil mill operators have traditionally relied on open ponding systems.[8] Nevertheless, these systems demand substantial land areas and prolonged treatment times (up to 40−60 days), resulting in unpleasant odors and making them less effective for low-concentration POME.[9] As such, advanced oxidation processes (AOPs) have been selected as an effective method for POME treatment, utilizing reactive oxygen species (ROS) to efficiently photodegrade pollutants in an environmentally friendly manner.[10]

Among the AOPs, photocatalysis represents one of the most promising methods due to its effectiveness in treating diverse types of wastewater.[11] This technique performed under mild conditions is able to convert organic wastewater pollutants into water (H_2O), carbon dioxide (CO_2), or smaller molecules. Furthermore, it can reduce or oxidize inorganic pollutants into benign compounds.[12] As a result, photocatalysis has been considered as a sustainable alternative approach for the degradation of organic pollutants.[13,14] The synthesis of photocatalysts is usually performed using various elements, including nonmetals and metalloids, which are chosen based on their specific chemical and physical properties for optimized performance.[14] Several examples of photocatalysts, i.e., titanium(IV) oxide (TiO_2), zinc oxide (ZnO), graphitic carbon nitride (g-C_3N_4), and metal-based catalysts, have been widely investigated for their applications in photocatalysis. Among them, TiO_2 has received considerable attention over the past two to three decades as efficient photocatalysts and photoanodes. Moreover, they have been implemented in advancing dye-sensitized solar cells (DSSCs) and in the elimination of pollutants.[15,16]

TiO_2 is a nontoxic, low-cost, chemically stable, biocompatible, and effective oxidizing agent with a wide surface area. This transition metal oxide is regarded as a good material for photocatalysis due to its broad energy band gap.[17] This is related to its numerous benefits, including optical quality and chemical and thermal stability. Because of its greater surface area per unit volume than bulk materials, TiO_2 nanostructures show higher rates of photocatalytic reactions. Many potential uses of TiO_2 have been documented, including solid waste management, sewage treatment, air purification, antibacterial disinfection, and self-cleaning.[18,19] The photocatalytic process begins with the existence of e^-−h^+ pair reaction, including holes in the valence band (VB) and conduction band (CB) as shown in Figure 1.

However, TiO_2 has several drawbacks as well, such as its broad energy band gap (3.2 eV), quick recombination of photogenerated charge carriers, and minimal light absorption area,[20] which will impact its catalytic efficiency. To minimize this constraint, the codoping of TiO_2 is employed to improve its photocatalytic activity due to the presence of synergistic effects between the codopants. Furthermore, the incorporation of codopants to the structure may reduce TiO_2's broad band gap (3.2 eV). A transition from ultraviolet (UV) to visible light will occur, resulting in slow e^-−h^+ pair recombination, thereby enhancing the photocatalytic activity.[21] For instance, the introduction of manganese (Mn) codopant into black TiO_2 decreased the band gap of TiO_2 NPs, extending its light absorption to the visible light region, and improved the

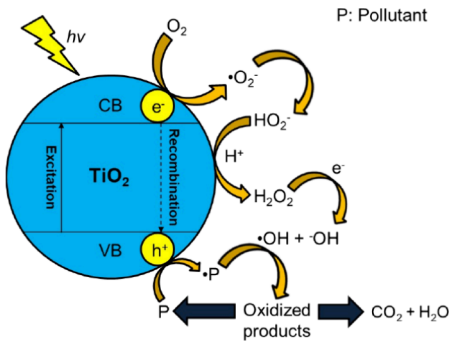

Figure 1. Photocatalytic degradation process utilizing TiO_2.

removal of treated POME along with COD to 86.0% and 88.87%, respectively.[22] In another study, the synergistic effect of silver (Ag) and iron (Fe) in Ag, Fe codoped TiO_2 showed better visible light response and enhanced photocatalytic performance of methylene blue (MB) dye with a maximum degradation of 80.22% for the sample with the highest Ag concentration after 180 min of reaction.[23]

Therefore, in this study, the limitations of TiO_2 are addressed by the synthesis of carbon, nitrogen codoped titanium oxide nanoparticles (C, N-TiO_2 NPs) via a sol−gel approach for the treatment of POME. The sol−gel technique is the most commonly used technique for the synthesis of C, N-TiO_2 NPs as it is an economical and simple operation process that produces high-purity products in comparison to other methods, such as ultrasonication and hydrothermal processes, which involve high costs of equipment and low efficiency for synthesis in a wide scale.[24,25] The C, N-TiO_2 NP photocatalyst was synthesized at low temperatures using titanium(IV) isopropoxide (TTIP) as a precursor, carboxymethyl cellulose (CMC) as a C precursor, and urea as a N precursor. The photocatalytic activity of the synthesized C and N-TiO_2 NPs was then studied by photodegradation of POME as a model pollutant under visible light.

2. RESULTS AND DISCUSSION

2.1. Characterization of Synthesized C, N-TiO_2 NPs.

2.1.1. X-ray Diffraction (XRD). The crystalline phases and structure of the C and N-TiO2 NPs were determined by XRD analysis. The XRD patterns of the synthesized photocatalyst as shown in Figure 2 indicate the broadening of the Bragg peaks, suggesting a relatively small crystallite size. According to the crystallography open database (COD) file no. 5000223, the diffraction peaks located at 2θ values of 25.29, 37.84, 48.01, 53.94, 54.56, 62.65, 68.74, 70.25, and 75.16° correspond to reflections of the (101), (004), (200), (105), (211), (204), (116), (220), and (215) planes, respectively, confirming the presence of the tetragonal anatase phase of C, N-TiO2 NPs. These peaks detected were similar to those of bulk anatase TiO_2 as reported in one study.[26] Calcination of the TiO2 NPs at 500 °C resulted in the formation of the anatase phase, which is consistent with the findings from Mohamad Idris and coworkers.[27] This process resulted in sharper and more intense peaks, indicating an increase in crystallinity.[28] By using the Scherrer formula (eq 1), the average crystallite size was calculated to be 11.35 nm based on the most intense (101) diffraction peak of anatase TiO_2.

$$\tau = \frac{K\lambda}{\beta \cos\theta} \quad (1)$$

https://doi.org/10.1021/acsomega.4c08813
ACS Omega 2025, 10, 2858−2870

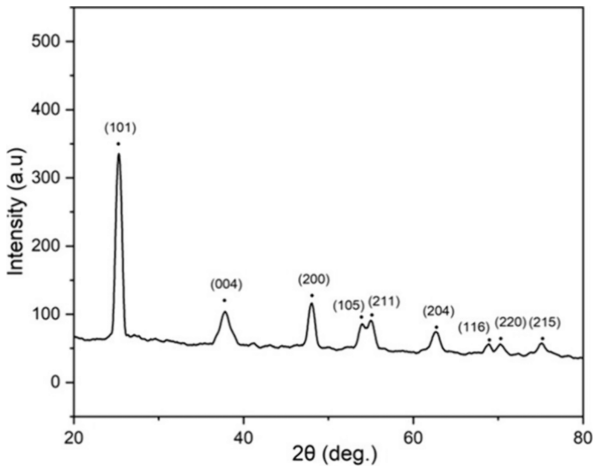

Figure 2. XRD for the synthesized C, N-TiO2 NPs with the Miller indices of the reflections (COD file no. 5000223). Adapted with permission from Mohamad Idris et al., (2024). C, N-Codoped TiO_2 Nanoparticles Immobilized on Floating Alginate Beads for Diazinon Removal under Solar Light Irradiation. *ACS Appl. Nano Mater.* **2024**, 7(16), 18273−18286. Copyright 2024, American Chemical Society. 10.1021/acsanm.3c03622.

where τ is the average crystallite size of the solid particle, K is the Scherrer constant (0.9), λ is the X-ray wavelength (0.154), β is the full width at half-maximum intensity (fwhm), and θ is the diffraction angle.

2.1.2. Fourier Transform Infrared (FTIR) Spectroscopy. The chemical composition of the synthesized C, N-TiO_2 NPs was determined by FTIR analysis. The FTIR spectrum of the C, N-TiO_2 NPs is illustrated in Figure 3, and the assigned

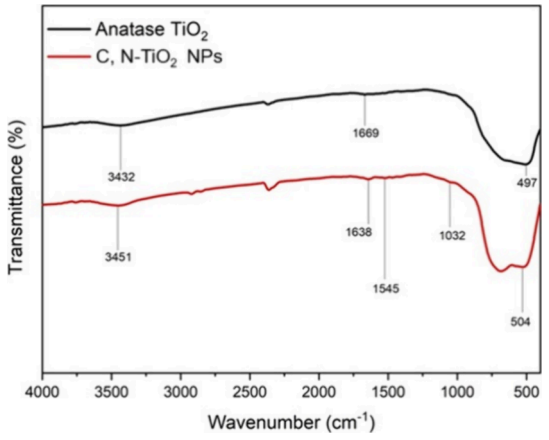

Figure 3. FTIR spectrum of anatase TiO_2 and synthesized C, N-TiO_2 NPs.

peaks are summarized in Table S1. According to Figure 3, the broad band between 3500 and 2400 cm^{-1} was attributed to the −OH bending and stretching of C, N-TiO_2 NPs.[29] The stretching and bending vibrational modes of the hydroxyl group (−OH) on the oxide surface at 3451 cm^{-1} are indicated in this spectrum. The Ti−OH bending vibration was observed from the peak at 1638 cm^{-1}. Additionally, the strong absorption band at 1545 cm^{-1} is assigned to the stretching vibration of the C−N bond, confirming the successful doping of N into the TiO_2 lattice.[30] The peak at 1032 cm^{-1} is assigned to the bending of the N−Ti group. Moreover, the FTIR spectrum typically displays peaks at 504 cm^{-1} for the Ti−O and Ti−O−Ti bonds. The presence of these functional groups in the FTIR spectrum consequently verified that the sol−gel method of C, N-TiO_2 NP production was successful.

2.1.3. High-Resolution Transmission Electron Microscopy (HRTEM). HRTEM analysis was used to determine the shape and size distribution of the synthesized C, N-TiO2 NPs. Figure 4a,b displays the arrangements of irregular, spherical, and aggregated particles as observed in the gray shadow region (Figure 4a) due to high surface energy of the smaller particle size. The average particle size of the photocatalyst was calculated to be 15.55 ± 2.67 nm (Figure 4d), which showed a slight difference from that determined by XRD. This is because the particle size measured by HRTEM is based on the direct visual measurement of microscopic images, while the fwhm of the most intense peak is taken into consideration for particle size determination by XRD. Several factors may contribute to the discrepancy in the average particle size value including broad size distribution, shape factor, polycrystallinity, and polydispersity.[31] Conversely, the interplanar distance of the synthesized C, N-TiO_2 NPs from the lattice fringes in the high magnification image of Figure 4c was measured to be 0.36 nm, which corresponded to the anatase phase. The lattice fringes were calculated by using the fast Fourier transform (FFT) image of a particular region, as illustrated in the inset of Figure 4c.

The crystallite size of the synthesized C, N-TiO_2 NPs was found to be larger than that for the undoped TiO_2 due to the codoping of C and N into the TiO_2 lattice.[26] Atoms with a smaller radius require less energy to be substituted than those with a larger radius.[32] As a result, because N atoms have smaller radii than oxygen (O) atoms, they can easily replace O atoms in the TiO_2 lattice, leading to the substitutional doping.[33] Meanwhile, C atoms, due to their larger atomic radii than N and O atoms, are challenging to incorporate into the TiO_2 lattice. Consequently, they tend to reside on the surface, forming a carbonated species layer. This surface layer, called interstitial doping, enlarges the TiO_2 crystals.[34] Furthermore, the synergistic effect between C and N dopants enhances the photocatalytic performance of C, N-TiO_2 NPs in degrading pollutants.[35]

2.1.4. X-ray Photoelectron Spectroscopy (XPS). The overall chemical composition and environment of the C, N-TiO_2 NPs were examined by XPS analysis. Figure 5a−d displays the Ti 2p, O 1s, C 1s, and N 1s XPS spectra of the synthesized NPs, respectively, which were deconvoluted using Gaussian line fitting via Origin, and their binding energy (BE) values are tabulated in Table S2. The presence of the Ti 2p peaks detected at BE of 459.21 and 464.96 eV for the Ti $2p_{3/2}$ and Ti $2p_{1/2}$ regions, respectively, in Figure 5a corresponds to the orbital spin doublet of the Ti^{4+}−O bonds in the C, N-TiO_2 NPs. The positions of these peaks at a relatively higher BE than those in pure anatase phase TiO_2 containing Ti^{4+}−O bonds as reported in previous studies[36] may be due to the introduction of C and N into the TiO_2 lattice, which is associated with the different coordination environment of the Ti and O atoms.[37]

The O 1s spectrum in Figure 5b depicts two peaks at 529.41 and 530.91 eV, which are ascribed to the lattice oxygen (O_L) in TiO_2 and surface adsorbed −OH groups, respectively. The absence of the peak (suboxide oxygen) between the two existing peaks may indicate the formation of TiO_2 along with some mixed oxide during the codoping process.[38] From the high-resolution deconvoluted C 1s spectrum of C, N-TiO_2

https://doi.org/10.1021/acsomega.4c08813
ACS Omega 2025, 10, 2858−2870

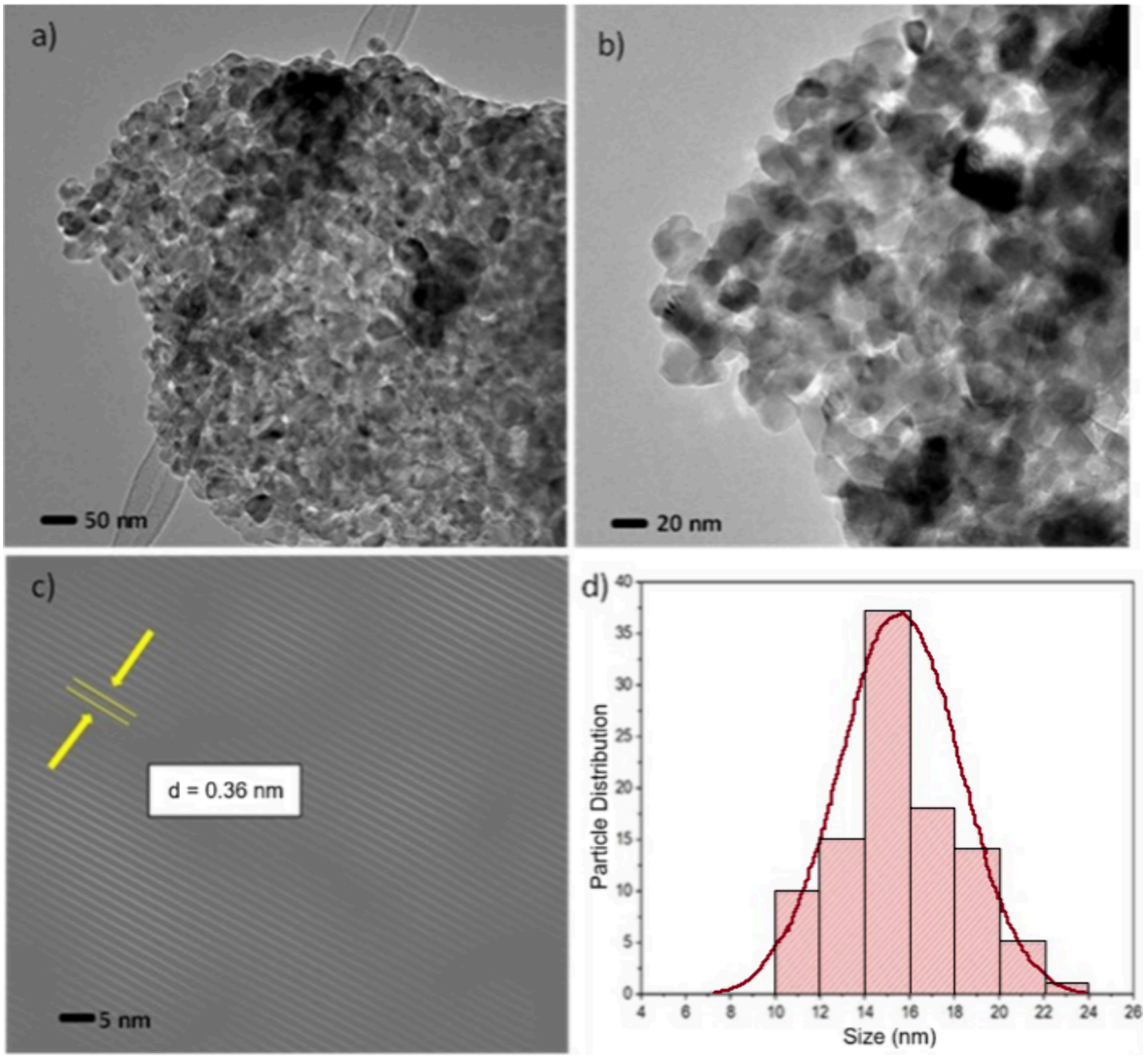

Figure 4. HRTEM images of synthesized C, N-TiO_2 NPs at (a) low magnification of 50 nm and (b) 20 nm and at (c) high magnification of 5 nm with inlay displayed. The FFT image corresponds to the specified area. (d) Particle size distribution of C, N-TiO_2 NPs.

(Figure 5c), three peaks are located at BE of 285.61, 286.86, and 289.61 eV. These peaks each represents the C−C bond that is attributed to the adventitious elemental carbon, C−O bond, and C═O bond, respectively, which are derived from the substitution of the lattice Ti atoms with the formation of Ti−O−C bonds.[37,39] The deconvolution of the N 1s spectrum of C, N-TiO_2 (Figure 5d) reveals the existence of four peaks in the range of 399−404 eV. The existence of two peaks at 400.21 and 401.11 eV are attributed to the substitutional N doping (O−Ti−N), which plays a major role in the modification of the electrical conductivity (EC) and band gap narrowing of the TiO_2 by elevation of the valence band (VB).[40] Conversely, the peaks at >402 eV are due to the chemical absorption of N on the TiO_2 surface. This indicates that the detection of the peaks at 402.61 and 403.41 eV may suggest the occurrence of the interstitial N doping in the TiO_2 lattice (Ti−O−N),[37] which only introduces some isolated localized N 2p states in the band gap.[40]

2.1.5. Optical Properties of Anatase TiO_2 and C, N-TiO_2 NPs. The band gap energies of synthesized C, N-TiO_2 NPs and anatase TiO_2 were determined using ultraviolet−visible diffuse reflectance spectroscopy (UV−vis DRS). Figure 6a shows the absorption spectrum of the synthesized C, N-TiO_2 NPs and anatase TiO_2, while its inset depicts the band gap as determined by the Kubelka−Munk theory. By extrapolation of the linear region of the graph of $(k h\nu)^{1/2}$ versus photon energy in the wavelength range 200−800 nm, the energy of the band gap was calculated. The absorbance maximum was observed at <400 nm for anatase TiO_2 with a band gap of 3.2 eV and 414 nm for C, N-TiO_2 NPs, corresponding to a band gap of 2.95 eV.

However, the introduction of codopants (C and N) into TiO_2 altered its light absorption properties, shifting the absorption from the UV region into the visible light region.[27] This also resulted in the reduction of the band gap to 2.95 from 3.2 eV for anatase TiO_2. Additionally, the introduction of C and N, which serve as impurities that induce electronic defects in TiO_2, is responsible for the generation of new energy levels that are located below the CB, causing a decrease in band gap energy.[41] In the process of photocatalysis, the reduction in band gap energy suggests that C, N-TiO_2 NPs may be able to perform in the visible light region.

Figure 6b illustrates the photoluminescence (PL) spectra of anatase TiO_2 and C, N-TiO_2 NPs under 325 nm excitation

https://doi.org/10.1021/acsomega.4c08813
ACS Omega 2025, 10, 2858−2870

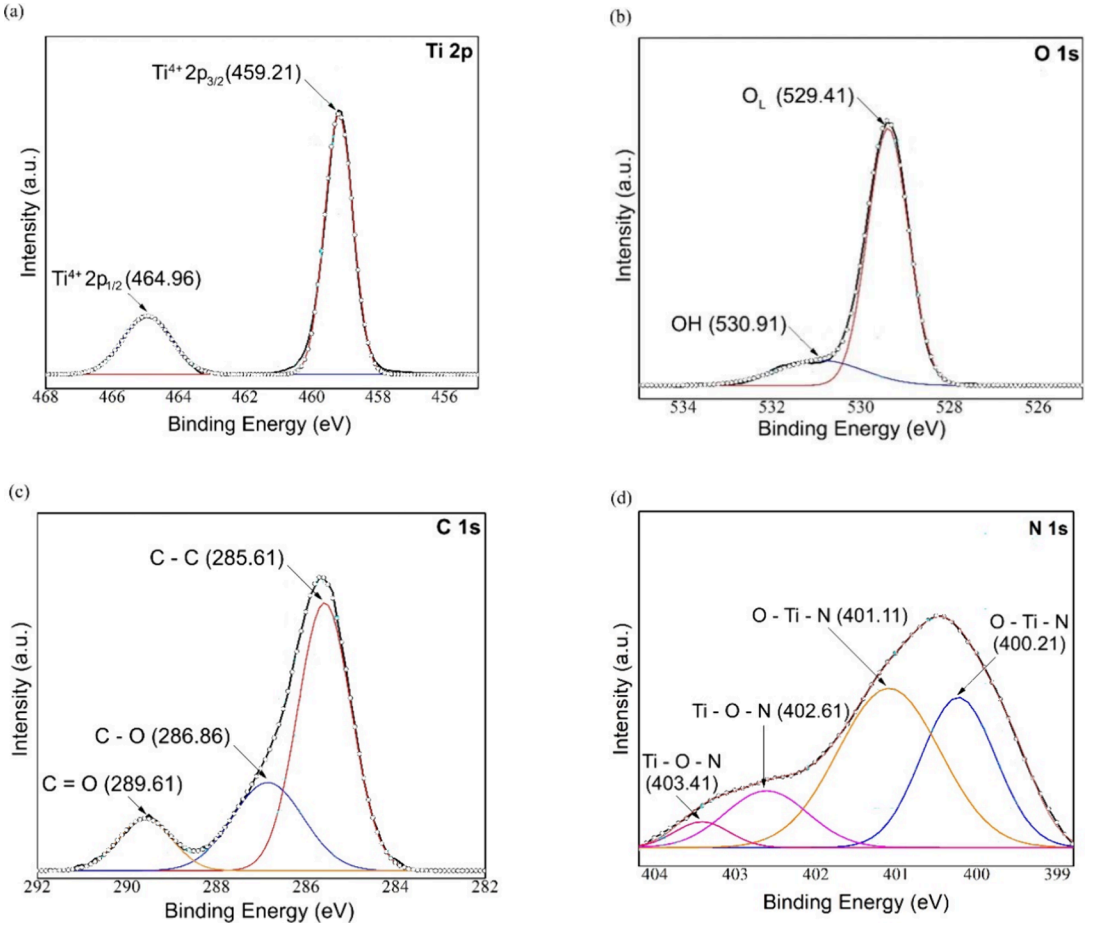

Figure 5. High-resolution deconvoluted (a) Ti 2p, (b) O 1s, (c) C 1s, and (d) N 1s XPS spectra of C, N-TiO_2 NPs.

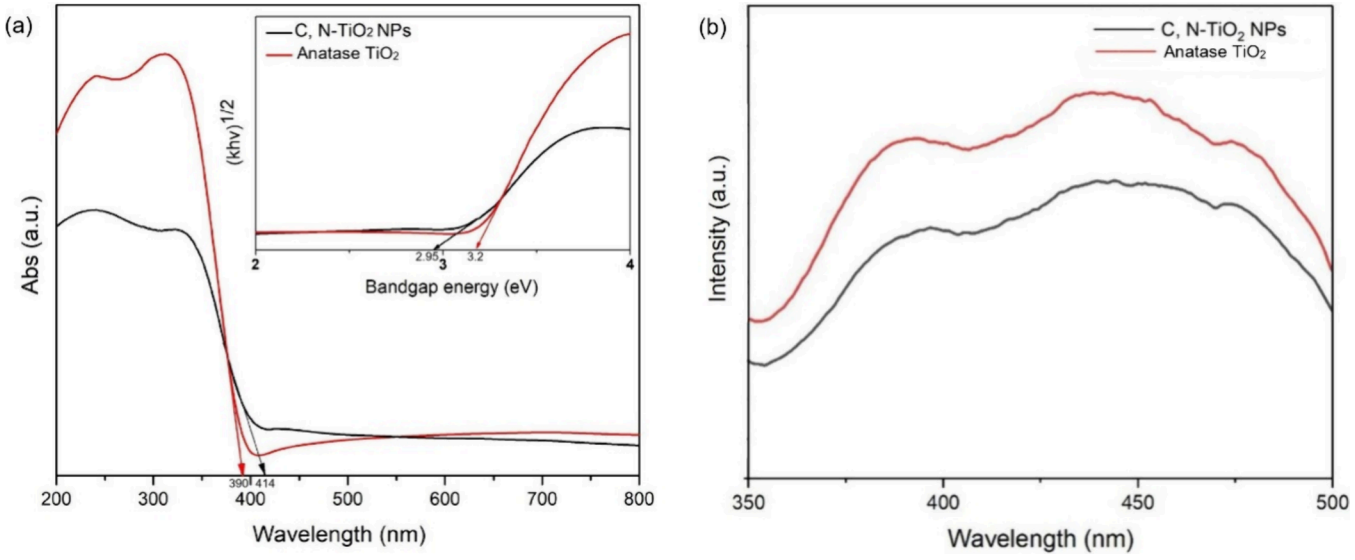

Figure 6. (a) Band gap spectrum of C, N-TiO_2 NPs and anatase TiO_2 with the inset showing the absorption of C, N-TiO_2 NPs and anatase TiO_2. (b) PL spectra of the synthesized C, N-TiO_2 NPs and anatase TiO_2.

wavelength and 10 s acquisition time. A broad emission is detected in the 350 to 500 nm spectral range. The emission spectrum profile displays the highest intensity at around 440 nm, indicating a charge-transfer transition of Ti^{4+} before the recombination of trapped e^-−h^+ in TiO_2.[27] The lower intensity of C, N-TiO_2 NPs in comparison to anatase TiO_2 suggests a slower recombination rate of e^-−h^+ pairs and higher photocatalytic activity of the photocatalyst. As reflected by the work of Chen and co-researchers, the high photocatalytic activity was related to the separation and migration efficiency of photogenerated carriers based on the investigation of the carrier recombination by PL and electrochemical impedance

https://doi.org/10.1021/acsomega.4c08813
ACS Omega 2025, 10, 2858−2870

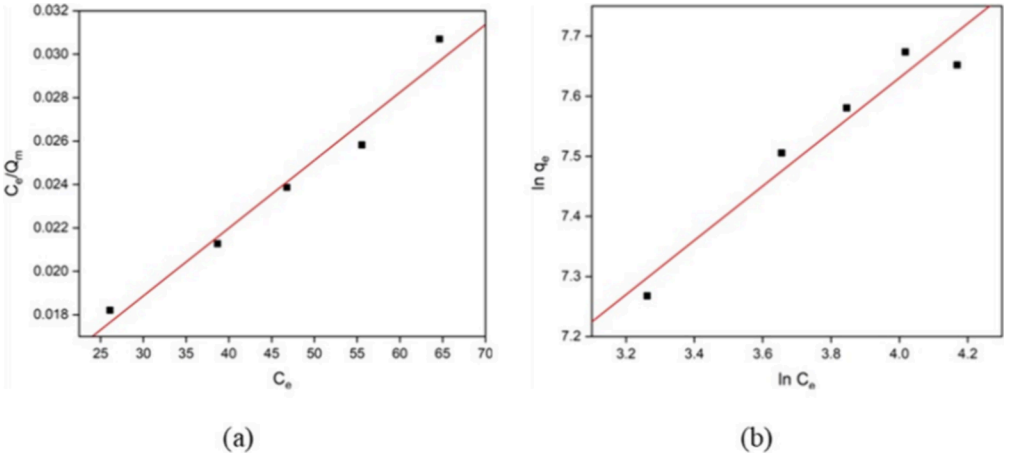

Figure 7. Adsorption capacity of C, N-TiO_2 NPs for the (a) Langmuir isotherm of variation adsorption (C_e/q_m) against the equilibrium concentration (C_e) and (b) Freundlich isotherm of variation adsorption (ln q_e) against the equilibrium concentration (ln C_e).

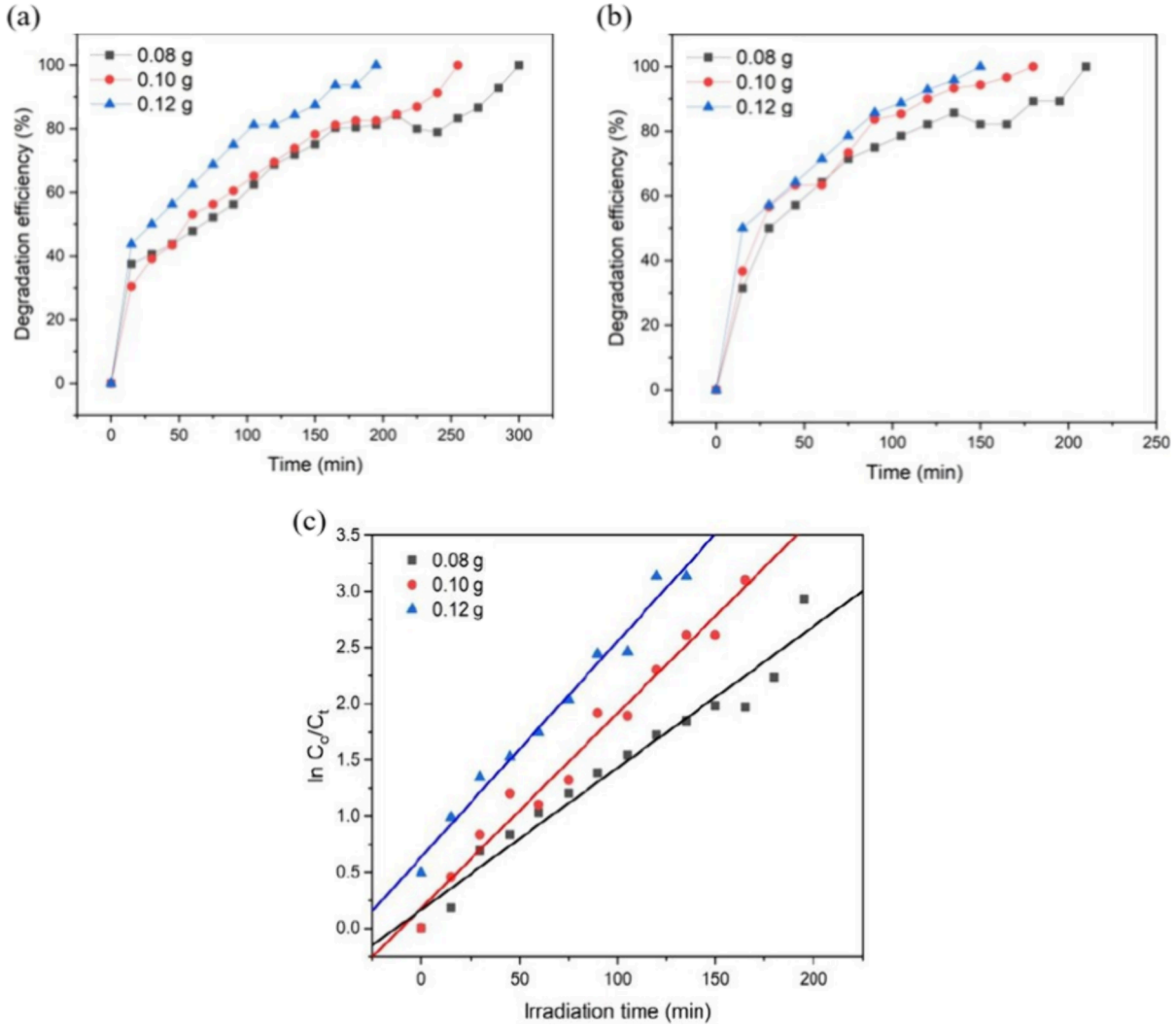

Figure 8. Catalyst dosages of 0.08, 0.10, and 0.12 g for the degradation efficiency of POME (a) by anatase TiO_2 and (b) by C, N-TiO_2 NPs under solar light irradiation. (c) First-order kinetics for the degradation of POME by C, N-TiO_2NPs with catalyst dosages of 0.08, 0.10, and 0.12 g.

spectroscopy (EIS), whereby the lower PL intensity of C, N-TiO_2 indicates that the sample has a higher carrier separation efficiency.[42] The presence of codopants (C and N) in C, N-TiO_2 NPs suppresses the energy-wasting charge recombination process, thereby promoting the separation of photoinduced carriers.[26]

2.2. Adsorption Studies of C, N-TiO_2 NPs. The adsorption capability of C, N-TiO_2 NPs and their interaction

https://doi.org/10.1021/acsomega.4c08813
ACS Omega 2025, 10, 2858−2870

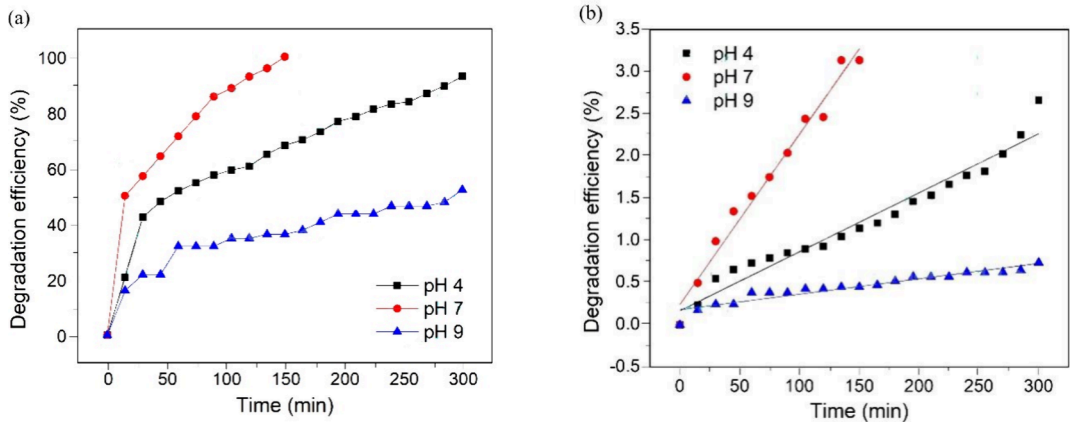

Figure 9. (a) Degradation efficiencies of POME and (b) their first-order kinetics with various initial pH values of POME by optimized C, N-TiO_2 NPs under solar light irradiation.

with POME were determined through isotherm studies conducted under dark conditions. In this study, both the Langmuir and Freundlich isotherm models were utilized to evaluate the catalyst's maximum adsorption capacity. Figure 7 shows the graphs of the Langmuir and Freundlich adsorption isotherms, respectively, whereby the Langmuir isotherm is represented by a graph of C_e/q_m versus C_e, while the graph of ln q_e versus ln C_e corresponds to the Freundlich model.

According to the POME adsorption isotherm results, the R^2 value for the Langmuir model (0.962) was relatively higher than that for the Freundlich model (0.940). This indicates that the adsorption aligns well with the Langmuir isotherm model, thus implying that the adsorption process is homogeneous, whereby POME as the adsorbate is adsorbed in the form of a monolayer onto C, N-TiO_2 NPs as the adsorbent with adsorption taking place at a fixed number of adsorption sites without the occurrence of lateral interaction or transmigration of POME in the plane of the NPs.[43] The greater number of active sites available on the NPs prior to its nanosize characteristic might lead to a high adsorption capacity of POME. Additionally, the Langmuir adsorption isotherm assumes a uniform distribution of active sites across the particle surface, leading to a consistent and homogeneous adsorption response.[27]

Besides, the shape of an adsorption isotherm is an indication of the favorability of the adsorption process from the equilibrium parameter, R_L value of the Langmuir isotherm: favorable ($0 < R_L < 1$), unfavorable ($R_L > 1$), or irreversible ($R_L = 0$), as calculated using eq 2:

$$R_L = 1/(1 + bC_e) \quad (2)$$

The obtained R_L value of 0.437 from eq 2 indicates that the adsorption was successful as the R_L value falls within the range of 0 and 1.

2.3. Photocatalytic Activities of the Catalyst against POME. *2.3.1. Effect of Catalyst Dosage.* The photocatalytic degradation of POME was investigated using solar light irradiation with both anatase TiO_2 and C, N-TiO_2 NPs. POME was chosen as the pollutant as it contains a mixture of organic and inorganic substances that pose severe environmental challenges if not properly treated.[44]

In this experiment, the photocatalytic degradation of POME was studied with varying catalyst dosages (0.08, 0.10, and 0.12 g), as shown in Figure 8a,b, to investigate the optimal dosage of POME degradation under solar light irradiation. The COD resulted in concentration values for the three dosages of both photocatalysts, which can be referred to in Table S3. The POME removal efficiency was calculated using eq 3.

$$R = (C_0 - C_t)/C_0 \times 100\% \quad (3)$$

where C_0 is the initial concentration of POME and C_t is the concentration of POME during irradiation.

From the results obtained, POME degradation efficiencies of 100% were achieved in 300 and 255 min with anatase TiO_2 dosages of 0.08 and 0.10 g, respectively, while complete POME degradation times of 210 and 180 min were recorded for C, N-TiO_2 NPs dosages of 0.08 and 0.10 g, respectively. In contrast, the complete degradation of POME with 0.12 g of anatase TiO_2 was achieved at 195 min, whereas a similar catalyst dosage of C, N-TiO_2 NPs completely degraded POME at 150 min, thus indicating that the POME degradation time using C, N-TiO2 NPs is the shortest. This demonstrated that the unique traits of C, N-TiO_2 NPs resulted in the enhancement of the photocatalytic performance in degrading POME.

The trend of POME degradation rate increases with the rise of catalyst dosage from 0.08 to 0.12 g, attributed to the expanded active surface area of the catalysts. Nevertheless, increasing the catalyst dosage beyond 0.12 g would lead to an increase in the turbidity of the suspension, thus reducing the penetration of light. This would in turn result in a decrease in the rate of utilization of light.[45] Therefore, 0.12 g was selected as the optimum catalyst dosage for balancing the effectiveness, thus accounting for the minimum usage of excessive catalyst and generation of potential secondary pollutants, aligning with the Green Chemistry principles.

Figure 8c depicts the first-order kinetic model's graph used for the kinetic analysis of photocatalytic degradation of POME by C, N-TiO_2 NPs. Rate constants (k) were derived from the slopes of linear plots $\ln(C_0/C_t)$ against time. The obtained results for k were 0.013, 0.017, and 0.019 min^{-1} with R^2 values of 0.960, 0.976, and 0.981 for catalyst dosages of 0.08, 0.10, and 0.12 g, respectively, as tabulated in Table S4. Therefore, these results indicated that the C, N-TiO_2 NPs displayed the best photocatalytic performance at 0.12 g of catalyst dosage with the highest value of the photodegradation rate.

2.3.2. Effect of Various Initial pH Values of POME. In this study, the effect of pH values of 4, 7, and 9 toward the degradation of POME was investigated by adjustment using 1.5 M NaOH and 2% acetic acid solutions using optimized C, N-TiO_2 NPs. Similar to the study of the effect of catalyst

https://doi.org/10.1021/acsomega.4c08813
ACS Omega 2025, 10, 2858−2870

dosage, the COD analysis was employed in the determination of the concentrations of degraded POME for the three pH values, and the data are tabulated in Table S5. The patterns of the degradation efficiencies and first-order kinetics are displayed in Figure 9 and Table S6, respectively. The values of k determined from the slopes of linear plots $\ln(C_0/C_t)$ against time were 0.007, 0.019, and 0.002 min^{-1} with R^2 values of 0.958, 0.981, and 0.905 for pH values of 4, 7, and 9, respectively. From the results obtained, the photocatalytic process differed according to the following trend: pH 7 > pH 4 > pH 9, whereby complete degradation (100.00% within 150 min) was achieved under neutral conditions with the highest k (0.019 min^{-1}) obtained compared to those for pH 4 (92.99% for 300 min, k = 0.007 min^{-1}) and pH 9 (52.17% for 300 min, k = 0.002 min^{-1}). This showed that the photocatalytic degradation of POME was favored at pH 7 in contrast to both acidic and basic conditions (pH 4 and 9), indicating that the degradation efficiency is significantly influenced by pH as this parameter determines the nature of the charge on the surface of the C, N-TiO_2 photocatalyst through the adoption of point of zero charge (PZC),[46] whereby the PZC = 6−8 depending on the TiO_2 sample.[47] For instance, when pH = PZC on the surface of the photocatalyst, there is little or no interaction between the POME contaminants and the photocatalyst due to the absence of electrostatic interactions.[46] However, at pH < PZC, the surface of the photocatalyst is positively charged, which will then gradually receive electrons by POME adsorbed to the C, N-TiO_2-activated photon to undergo different photocatalytic reactions, thereby reducing the degradation efficiency of POME. On the other hand, when pH > PZC, the negatively charged surface of the photocatalyst rejects anions in water, thus inhibiting the photocatalytic process.[46,47] As a result, it can be concluded that pH 7 is the most promising pH condition for the degradation of POME as it exhibits complete degradation in the shortest time.

2.4. Mineralization Study. The total organic carbon (TOC) analyzer plays a central role by accurately measuring the total amount of organic C present in C, N-TiO_2 NPs, which is essential for assessing the degree and efficiency of the mineralization of POME. The samples were taken at 0 min before and 150 min after exposure to solar light. According to the obtained result, only 58.14% of POME was mineralized during photocatalytic activity. However, the TOC removal has a lower value than the degradation of POME conducted using COD, whereby this method degraded 100% of POME within 150 min. Due to this occurrence, it can be deduced that there is no complete degradation of CO_2 and H_2O.[48] As a result, it is concluded that the breakdown of smaller organic molecules involves their complete oxidation to CO_2, which is based on the TOC result.

2.5. Scavenging Study. The reactive species, including reactive oxygen species (ROS) such as superoxide radicals ($\bullet O_2^-$) and hydroxyl radicals (•OH) and photogenerated holes (h^+) or e^- involved in the degradation of POME under solar light irradiation, were studied through a scavenging test to assess the probable reaction pathways. In the photodegradation of POME, h^+, $\bullet O_2^-$, and •OH are notable. Acetonitrile (CH_3CN), methanol (CH_3OH), and silver nitrate ($AgNO_3$) were utilized in this study as scavengers for •OH, h^+, and $\bullet O_2^-$, respectively. Figure 10 depicts the free radical scavenging in the photodegradation of POME. During the degradation of POME in the presence and absence of scavengers, $AgNO_3$ limited the degradation of POME with

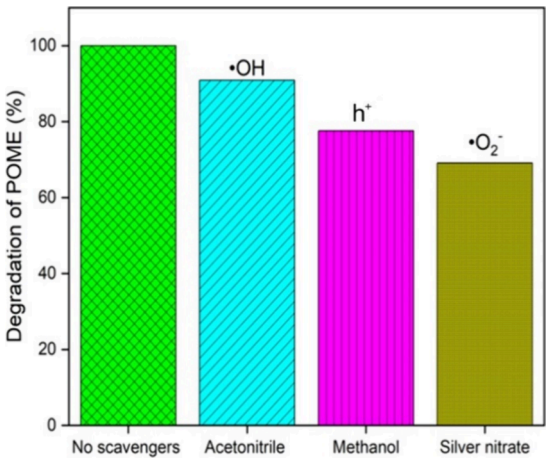

Figure 10. Radical scavenging test of the optimized C, N-TiO_2 NPs.

the highest reduction, which is 69.15%, followed by CH_3OH with 77.6% and CH_3CN with 90.9% of POME removed. Moreover, the use of $AgNO_3$ in this study also provides a scavenging effect that is similar to that of e^-, whereby $AgNO_3$ acts as an e^- trapping agent, thus reducing O_2 in the generation of $\bullet O_2^-$, which is in good agreement according to one study.[49] As such, this observation suggests that $\bullet O_2^-$ is predominant and plays a crucial role in the photocatalytic activity of the POME.

2.6. Proposed Mechanism for POME Degradation. The photocatalytic performance of semiconductor-based photocatalysts is critical for their ability to separate charges. Based on the previous scavenging test observation, $\bullet O_2^-$ is more prominent in the photodegradation of POME, followed by h^+ and •OH. It is thus crucial to provide a mechanism for the degradation of POME. Equation 4 describes the promotion of photoexcited e^- from VB to CB during the photocatalytic process of C, N-TiO_2 NPs, resulting in the formation of an e^-−h^+ pair. As shown in eq 5, $\bullet O_2^-$ plays an important role, and adsorbed O_2 will undergo degradation to $\bullet O_2^-$ in the CB. From eq 6, $\bullet O_2^-$ breaks down the POME molecule into harmless chemicals such as CO_2 and H_2O. Furthermore, the $\bullet O_2^-$ will undergo reactions with protons (H^+) present in solution to form H_2O_2, which is responsible for POME degradation based on eqs 7 and 8. Moreover, according to eqs 9 and 10, h^+ is expected to produce •OH, which converts POME into CO_2 and H_2O. In this finding, $\bullet O_2^-$ and •OH are responsible for the breakdown of POME into CO_2 and H_2O, with $\bullet O_2^-$ playing the dominating role in the photocatalytic process. Equations 4−10 illustrate the potential pathways for POME degradation, with the scheme of the proposed degradation mechanism displayed in Figure 11.

$$\text{C, N} - \text{TiO}_2\text{NPs} + h\nu \rightarrow e_{CB}^- + h_{VB}^+ \quad (4)$$

$$O_2 + e_{CB}^- \rightarrow \bullet O_2^- \quad (5)$$

$$\bullet O_2^- + \text{POME} \rightarrow CO_2 + H_2O \quad (6)$$

$$\bullet O_2^- + 2H^+ \rightarrow H_2O_2 \quad (7)$$

$$H_2O_2 + h\nu + 2\text{OH}\bullet + \text{POME} \rightarrow CO_2 + H_2O \quad (8)$$

$$h_{VB}^+ + H_2O \rightarrow \bullet\text{OH} + 2H^+ \quad (9)$$

$$\bullet\text{OH} + \text{POME} \rightarrow CO_2 + H_2O \quad (10)$$

https://doi.org/10.1021/acsomega.4c08813
ACS Omega 2025, 10, 2858−2870

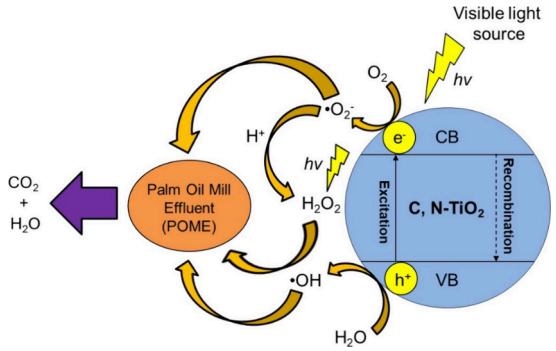

Figure 11. Proposed mechanism scheme for the photocatalytic degradation of POME.

2.7. Reusability of the C, N-TiO_2 Photocatalyst. The reusability test was conducted in five cycles of photocatalytic degradation of POME under identical experimental conditions, as shown in Figure 12, to examine the efficiency of repeated use of the optimized C, N-TiO_2 NPs. Figure 12 depicts that the degradation efficiency of POME decreased by 8.69%, from 98.68 to 89.99%, after being reused five times. The initial cycle resulted in 98.68% POME removal, indicating that the removal efficiency decreased by 1.32%. Due to a minor loss of photocatalytic activity for the following five cycles, it is proven that the C, N-TiO_2 NPs exhibit good stability during the photodegradation of POME under light irradiation. This relatively small drop is likely caused by the active site and the low adsorption ability of the photocatalyst. Furthermore, frequent washing, centrifugation, and usage may lead to the loss of the catalyst materials.[50] Therefore, the finding suggests that the C, N-TiO_2 NPs have good reusability, which plays a major role for wastewater treatment applications.

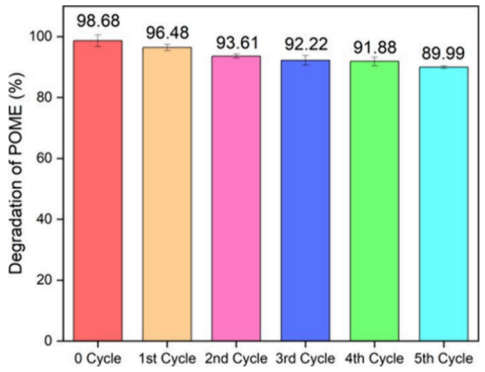

Figure 12. Reusability test of optimized C, N-TiO_2 NPs for five cycles (n = 2).

2.8. Comparative Discussion of the Present Work with the Reported Literature. In recent decades, the development of highly efficient semiconductors as photocatalysts for the degradation of POME has attracted considerable attention due to several benefits such as eco-friendliness, high efficiency, and low energy requirement. This method encompasses several crucial aspects, such as the types of materials employed, their band gap energies, and the degradation times and efficiencies after the degradation process. The comparison of this present study with several literature surveys related to the photocatalytic degradation of POME with semiconductor photocatalysts irradiated using a commercialized 300 W xenon lamp source is tabulated in Table 1. From Table 1, it is observed that the photocatalysts used in other reported studies were found to have lower catalytic performance than that in the current work in terms of their degradation times and efficiencies despite some of them possessing narrower band gaps than C, N-TiO_2. This was due to particle agglomeration, which decreases the surface-to-volume ratio, thus limiting the amount of incoming light radiation. This indicates that C, N-TiO_2 employed in this study has the potential to be efficient and economical for the photocatalytic treatment of POME.

Table 1. Photocatalytic Degradation of POME with Various Semiconductor Photocatalysts, Conditions, and Catalytic Performances[a]

photocatalyst	band gap energy (eV)	degradation time (min)	degradation efficiency (%)	reference
TiO_2/ biosilica	3.20	240	47	51
$CaFe_2O_4$	1.51	480	69	52
$BiVO_4$	2.50	240	24	53
C, N-TiO_2	2.95	150	100	this study

[a]All studies are comparable using a commercialized 300 W xenon lamp irradiation source.

3. CONCLUSIONS

C, N-TiO_2 NPs were successfully synthesized using the sol−gel method by employing TTIP, CMC and urea as a precursor for Ti, C, and N, respectively. XRD results showed that the C, N-TiO_2 NPs possessed a crystallite size of 11.35 nm, indicating high crystallinity and enhanced photocatalytic performance. The existence of the C−N−Ti group in the TiO_2 lattice was confirmed by the presence of the absorption bands at 1545 and 1032 cm^{-1} from FTIR analysis, proving the success of codoping of C and N. The presence of these elements was further clarified by XPS analysis indicating the substitutional and interstitial doping of N and C, respectively, into TiO_2. Optical studies revealed that the band gap of C, N-TiO_2 NPs was reduced from 3.2 to 2.95 eV from UV−vis DRS results, thus extending the adsorption of the photocatalyst to the visible light region. Meanwhile, PL indicated that the C, N-TiO_2 NPs had a lower intensity than anatase TiO_2, suggesting that slower e^-−h^+ pair recombination can improve photocatalytic efficiency. The adsorption isotherm studies of POME were compatible with the Langmuir isotherm model, as the Langmuir correlation coefficient R^2 of 0.962 was higher than the Freundlich R^2 value of 0.940. This suggested the occurrence of monolayer adsorption on the homogeneous sites of the pollutant. The photocatalytic degradation process of POME achieved maximum degradation efficiency (100%) under pH 7 using 0.12 g of the C, N-TiO_2 NPs. According to POME removal results from TOC studies, only about 58.14% of POME was degraded into CO_2 and H_2O in 150 min; the mineralization rate was significantly lower than the degradation rate because CO_2 and H_2O did not fully degrade. Scavenging studies showed that $\bullet O_2^-$ exhibited the highest activity in the photocatalytic degradation of POME. Moreover, the reusability of the C, N-TiO_2 NPs up to more than five cycles demonstrated that C, N-TiO_2 NPs are useful for the degradation of POME under solar light irradiation, which

https://doi.org/10.1021/acsomega.4c08813
ACS Omega 2025, 10, 2858−2870

makes them highly promising photocatalysts in wastewater treatment.

4. MATERIAL AND METHODS

4.1. Materials. Ammonia solution (NH_3) of 30% NH_4OH was purchased from Chemiz, Modern Lab, Malaysia. Titanium-(IV) isopropoxide (TTIP) with a purity of 97% was obtained from Sigma-Aldrich, Co., USA. Glacial acetic acid (CH_3COOH) and absolute ethanol (CH_3CH_2OH, 99.7%) were purchased from QReC, Modern Lab, Malaysia. Carboxymethylcellulose (CMC), sodium, and urea were obtained from Sigma-Aldrich, Modern Lab, Malaysia. Palm oil mill effluent (POME) was obtained from Sri Singgora Palm Oil Mill, Malaysia. Potassium dichromate ($K_2Cr_2O_7$). ammonium iron(II) sulfate-6-hydrate ($(NH_4)_2Fe(SO_4)_2 \cdot 6H_2O$), silver nitrate ($AgNO_3$), methanol ($CH_3OH$), and acetonitrile ($CH_3CN$) were purchased from Bendosen, Progressive Scientific, Malaysia. All chemicals were used as received without further purification.

4.2. Synthesis of C, N-TiO_2 NPs. The sol−gel method was utilized to synthesize C, N-TiO_2 NP photocatalysts, which was adopted from the previous study by Mohamad Idris et al.[27] Briefly, 25 mL of pure water was mixed with urea (3% N, 3 mmol), CMC (2% C, 2 mmol), and 4 mL of glacial CH_3COOH in beaker A. After 30 min, the solution was mixed. In the meantime, 25 mL of CH_3CH_2OH and 3 mL of TTIP were placed into beaker B and stirred for 30 min. Using a dropper, the solutions in beakers A and B were mixed one drop at a time for 60 min. Then, while stirring continuously for 30 min, ammonia solution (NH_4OH) was added to the mixture until the pH reached 9. Following a 10 min separation by centrifugation at 9000 rpm, the white precipitate underwent five washes with distilled water before being dried in an oven heated to 80 °C for a duration of 24 h. C, N-TiO_2 NPs were produced by heating the yellowish-gray powder in the furnace at 500 °C for 2 h.

4.3. Analytical and Characterization Techniques. The X-ray diffraction (XRD) analysis of the catalyst was carried out to evaluate its detailed crystal information, including the crystalline phase and crystallite size. The detailed crystalline information on the catalyst was obtained using XRD (PW 3040/60 X'PERT PRO, PANalytical, Netherlands), and the samples were analyzed using Cu Kα radiation (1.541 Å) in the range of 2θ = 15−105°. The crystallite size and crystallite phase of the catalyst were then determined. The data were analyzed using the XRD analysis PRO software tool (PANalytical, Netherlands). The chemical composition of the catalyst was evaluated using a Fourier transform infrared (FTIR) spectrometer (PerkinElmer Model System 2000, United States). Potassium bromide (KBr) powder and the sample were first weighed at a mass ratio of 1:10, ground in a mortar, and milled into a homogeneous powder. The powder was compressed into a thin and smooth surface pallet under 8−9 t of pressure. The FTIR spectrum was scanned in the range of 400 to 4000 cm^{-1}. High-resolution transmission electron microscopy (HRTEM, TECNAI G2 20 S- TWIN, FEI, Spain) was employed for the determination of the surface and morphology of the catalyst. In the sample preparation, 10 mg of the catalyst was dispersed in 10 mL of CH_3CH_2OH solvent by sonication. The distributed sample was then dried onto mesh C-coated grids, after which the images were captured at both low and high magnifications by using an acceleration voltage of 300 kV. Meanwhile, 100 particles were chosen from the obtained HRTEM images to measure the average particle size using the free program ImageJ software (ImageJ 1.51j8, USA). XPS analysis was performed for the catalyst with an X-ray photoelectron spectrometer (ESCA, AXIS ULTRA, Kratos Analytical, Shimadzu Group). The XPS spectra were excited by using a monochromatic Al Kα X-ray radiation source. Instrument calibration was carried out using a C 1s correction at 285.81 eV. UV−vis DRS was used to measure the synthesized material's band gap changes and shifts in the wavelength. The spectra were measured on a PerkinElmer Lambda 35 (USA) instrument equipped with a Labsphere RSAPE-20 integration sphere and a diffuse reflectance standard. The band gap energy was obtained by extrapolating the linear section from the graph of $(k\nu)^2$ against photon energy throughout a wavelength range of 200−800 nm using the Kubelka−Munk formula. The photoluminescence (PL) study was performed with a PerkinElmer LS 55 Luminescence Spectrometer (USA) with a 10 s acquisition time and a 325 nm excitation to investigate the behavior of charge carrier transfer and recombination process in the samples.

4.4. Adsorption Isotherm Studies. This study was conducted in the dark to determine the amount of solute that can be absorbed by the adsorbents. A total of 0.12 g of C, N-TiO_2 (optimized catalyst dosage) and 200 mL of POME solution (1, 5, 30, 50, and 75% of POME) were mixed at pH 7 (optimized pH) and stirred in the dark for 1 h. Every 10 min, the sample was regularly taken until the solution reached the equilibrium concentration, which was determined by chemical oxygen demand (COD) analysis. Moreover, the concentrations of POME in the solution for the initial and final adsorption were used to calculate the amount of POME absorbed.

4.5. Photocatalysis of POME. Before the photocatalytic reaction was conducted, the dark adsorption of the POME solution was first carried out for 60 min to achieve adsorption−desorption equilibrium. Different amounts of anatase TiO_2 and C, N-TiO_2 NPs (0.08, 0.10, and 0.12g) with an initial pH 7 of POME were prepared to treat the POME solution. Degradation of POME was performed under solar light irradiation (300 W xenon lamp) to investigate the photocatalytic activity of both catalysts. Upon exposure of the mixture to solar light, the degradation process was commenced. A light meter was used to measure the intensity of the solar light (luminosity between 80 and 100 klx). The COD reaction was used to analyze the photocatalytic activity of the samples collected every 15 min within a desired period. The photocatalysis process was repeated as above with 0.12 g of C, N-TiO_2 NPs for the investigation of the effect of pH toward POME degradation under pH values of 4 and 9.

4.6. Chemical Oxygen Demand (COD) Analysis. COD analysis was conducted to measure the concentration of the degraded POME solution in parts-per-million (ppm). The samples were prepared in each COD vessel by transferring 1.5 mL of digested solution using a micropipet followed by 2.5 mL of the POME sample collected during photocatalytic activity. Then, 3.5 mL of sulfuric acid (H_2SO_4) reagent was added into each vessel. The tube cap was tightened, and the vessel was inverted several times to allow complete mixing. After sample preparation, the vessels were placed in a heating block on a Hach DRB200 Digital COD Reactor preheated to 150 °C and refluxed for 2 h. The samples were then allowed to stand and cooled to room temperature. After that, the samples were transferred into a conical flask, two to three drops of ferroin

https://doi.org/10.1021/acsomega.4c08813
ACS Omega 2025, 10, 2858−2870

indicator solution were added, and titration was performed with standardized FAS. The end point was reached when one drop of the standardized FAS turned the color of the solution completely from blue-green to reddish brown. Similarly, a blank containing a reagent and distilled water was refluxed and titrated until its color turned to reddish brown.

4.7. Total Organic Carbon (TOC) Analysis. The degree of mineralization of treated POME was determined by using a TOC analyzer (Shimadzu, TOC-L). The samples obtained before and after the photocatalytic reaction were filtered with a nylon membrane filter with a pore size of 0.22 μm before the TOC analysis was performed. All the C's formed in the sample attributed to the presence of inorganic carbonates were converted to CO_2, which was then measured directly or indirectly before conversion into TOC or total carbon content.

4.8. Scavenging Study. The scavenging test was used to identify the reactive radical species that were involved in the photocatalytic degradation of POME. The reaction was carried out in the same manner as for the photocatalytic experiment in Section 4.4. CH_3OH (10% v/v), $AgNO_3$ (0.2 M), and CH_3CN (100% v/v) were implemented as scavengers to investigate the effects of h^+, $\bullet O_2^-$, and $\bullet OH$, respectively. The scavenging effect of $AgNO_3$ was similar to $\bullet O_2^-$.

4.9. Reusability of the Photocatalyst. The reusability of the C, N-TiO_2 photocatalyst was investigated for five cycles. Following the photocatalytic reaction, any pollutants or impurities were removed from the photocatalyst by centrifugation for 10 min at 9000 rpm in distilled water. Then, the sample was placed in an oven and dried overnight at 80 °C. The dried sample was collected and reused for the following photocatalytic activity.

■ ASSOCIATED CONTENT

Data Availability Statement

All the data that support the findings of this study are presented in the manuscript.

Supporting Information

The Supporting Information is available free of charge at https://pubs.acs.org/doi/10.1021/acsomega.4c08813.

> Peaks assigned from FTIR spectrum (Table S1); XPS fitting parameters for C, N-TiO_2 (Table S2); effect of catalyst dosage on the photocatalytic activity of C, N-TiO_2 NPs (Table S3); rate constants and correlation coefficients of degradation POME by C, N-TiO_2 NPs under solar light irradiation with different catalyst dosages (Table S4); effect of pH on the photocatalytic activity of C, N-TiO_2 NPs (Table S5); and degradation efficiencies, rate constants, and correlation coefficients of degradation POME by optimized C, N-TiO_2 NPs under solar light irradiation with different pH values (Table S6) (PDF)

■ AUTHOR INFORMATION

Corresponding Author

Hooi Ling Lee − *Nanomaterials Research Group, School of Chemical Sciences, Universiti Sains Malaysia, 11800 Minden, Penang, Malaysia*; orcid.org/0000-0002-9637-0617; Phone: +604-6533547; Email: hllee@usm.my; Fax: +604-6574854

Authors

Benjamin Tze-Wei Tan − *Nanomaterials Research Group, School of Chemical Sciences, Universiti Sains Malaysia, 11800 Minden, Penang, Malaysia*

Nor Ashikin Mohd. Rashid − *Nanomaterials Research Group, School of Chemical Sciences, Universiti Sains Malaysia, 11800 Minden, Penang, Malaysia*

Nurul Hidayah Mohamad Idris − *Nanomaterials Research Group, School of Chemical Sciences, Universiti Sains Malaysia, 11800 Minden, Penang, Malaysia*

Wee Long Wun − *i-Chem Solution Sdn. Bhd., 47160 Puchong, Selangor, Malaysia*

Complete contact information is available at: https://pubs.acs.org/10.1021/acsomega.4c08813

Author Contributions

The corresponding author contributed greatly to this article, and all authors contributed equally.

Notes

The authors declare no competing financial interest.

■ ACKNOWLEDGMENTS

This study was supported by the Fundamental Research Grant Scheme (R503-KR-FRG001-0000000656-K134), Ministry of Higher Education, Malaysia.

■ REFERENCES

(1) Madhav, S.; Ahamad, A.; Singh, A. K.; Kushawaha, J.; Chauhan, J. S.; Sharma, S.; Singh, P. Water Pollutants: Sources and Impact on the Environment and Human Health. In *Sensors in Water Pollutants Monitoring: Role of Material* Pooja, D.; Kumar, P.; Singh, P., Patil, S. (Eds.); Springer: Singapore, 2020; pp 43−62.

(2) Saad, M. S.; Wirzal, M. D. H.; Putra, Z. A. Review on current approach for treatment of palm oil mill effluent: Integrated system. *J. Environ. Manage.* **2021**, *286*, No. 112209.

(3) Lok, X.; Chan, Y. J.; Foo, D. C. Y. Simulation and optimization of full-scale palm oil mill effluent (POME) treatment plant with biogas production. *J. Water Process Eng.* **2020**, *38*, No. 101558.

(4) Anuar, M. A. M.; Amran, N. A.; Ruslan, M. S. H. Optimization of Progressive Freezing for Residual Oil Recovery from a Palm Oil-Water Mixture (POME Model). *ACS Omega* **2021**, *6* (4), 2707−2716.

(5) Mohd Yusof, M. A. B.; Chan, Y. J.; Chong, C. H.; Chew, C. L. Effects of operational processes and equipment in palm oil mills on characteristics of raw Palm Oil Mill Effluent (POME): A comparative study of four mills. *Clean. Waste Syst.* **2023**, *5*, No. 100101.

(6) Ranjit, P.; Jhansi, V.; Reddy, K. V. Conventional Wastewater Treatment Processes. In *Advances in the Domain of Environmental Biotechnology* Maddela, N. R.; Cruzatty, L. C. G.; Chakraborty, S. (Eds.); Springer: Singapore, 2021; pp 455−479.

(7) Crini, G.; Lichtfouse, E. Wastewater Treatment: An Overview. In *Green Adsorbents for Pollutant Removal* Crini, G., Lichtfouse, E. (Eds.); Springer International Publishing: Cham, 2018; pp 1−21.

(8) Tang, Y. M.; Tan, K. T.; Wong, L. P. Valorization of palm oil mill effluent via enhanced oil recovery as an alternative feedstock for biodiesel production. *Water Sci. Technol.* **2023**, *88*, 1404−1416.

(9) Ng, K. H. Adoption of TiO_2-photocatalysis for palm oil mill effluent (POME) treatment: Strengths, weaknesses, opportunities, threats (SWOT) and its practicality against traditional treatment in Malaysia. *Chemosphere* **2021**, *270*, No. 129378.

(10) Dihom, H. R.; Al-Shaibani, M. M.; Radin Mohamed, R. M. S.; Al-Gheethi, A. A.; Sharma, A.; Khamidun, M. H. B. Photocatalytic degradation of disperse azo dyes in textile wastewater using green zinc oxide nanoparticles synthesized in plant extract: A critical review. *J. Water Process Eng.* **2022**, *47*, No. 102705.

(11) Ren, G.; Han, H.; Wang, Y.; Liu, S.; Zhao, J.; Meng, X.; Li, Z. Recent advances of photocatalytic application in water treatment: A review. *Nanomaterials* **2021**, *11* (7), 1804.
(12) Li, Z.; Ji, S.; Liu, Y.; Cao, X.; Tian, S.; Chen, Y.; Niu, Z.; Li, Y. Well-Defined Materials for Heterogeneous Catalysis: From Nanoparticles to Isolated Single-Atom Sites. *Chem. Rev.* **2020**, *120* (2), 623−682.
(13) Li, C.; Yan, L.; Li, Y.; Zhang, D.; Bao, M.; Dong, L. TiO_2@palygorskite composite for the efficient remediation of oil spills via a dispersion-photodegradation synergy. *Front. Environ. Sci. Eng.* **2020**, *15* (4), 72.
(14) Akerdi, A. G.; Bahrami, S. H. Application of heterogeneous nano-semiconductors for photocatalytic advanced oxidation of organic compounds: A review. *J. Environ. Chem. Eng.* **2019**, *7* (5), No. 103283.
(15) Raguram, T.; Rajni, K. S. Synthesis and characterisation of Cu—Doped TiO_2 nanoparticles for DSSC and photocatalytic applications. *Int. J. Hydrogen Energy* **2022**, *47* (7), 4674−4689.
(16) Zandsalimi, Y.; Maleki, A.; Shahmoradi, B.; Dehestani, S.; Rezaee, R.; McKay, G. Photocatalytic removal of 2,4-Dichlorophenoxyacetic acid from aqueous solution using tungsten oxide doped zinc oxide nanoparticles immobilized on glass beads. *Environ. Technol.* **2022**, *43* (5), 631−645.
(17) Jetani, G. H.; Rahmani, M. B. TiO_2/GO nanocomposites: Synthesis, characterization, and DSSC application. *Eur. Phys. J. Plus* **2020**, *135* (9), 720.
(18) Wei, Y.; Wu, Q.; Meng, H.; Zhang, Y.; Cao, C. Recent advances in photocatalytic self-cleaning performances of TiO_2-based building materials. *RSC Adv.* **2023**, *13* (30), 20584−20597.
(19) Armaković, S. J.; Savanović, M. M.; Armaković, S. Titanium Dioxide as the Most Used Photocatalyst for Water Purification: An Overview. *Catalysts* **2023**, *13* (1), 26.
(20) Dharma, H. N. C.; Jaafar, J.; Widiastuti, N.; Matsuyama, H.; Rajabsadeh, S.; Othman, M. H. D.; Rahman, M. A.; Jafri, N. N. M.; Suhaimin, N. S.; Nasir, A. M.; Alias, N. H. (2022). A Review of Titanium Dioxide (TiO_2)-Based Photocatalyst for Oilfield-Produced Water Treatment. *Membranes* **2022**, *12* (3), 345.
(21) Gautam, J.; Yang, J.-M.; Yang, B. L. Transition metal co-doped TiO_2 nanotubes decorated with Pt nanoparticles on optical fibers as an efficient photocatalyst for the decomposition of hazardous gaseous pollutants. *Colloids Surf., A* **2022**, *643*, No. 128786.
(22) Nawaz, R.; Haider, S.; Anjum, M.; Oad, V. K.; Haider, A.; Khan, R.; Aqif, M.; Hanif, T.; Khan, N. Optimized photodegradation of palm oil agroindustry waste effluent using multivalent manganese−modified black titanium dioxide. *Environ. Sci. Pollut. Res.* **2023**, *30* (31), 77850−77874.
(23) Sukhadeve, G. K.; Bandewar, H.; Janbandhu, S. Y.; Jayaramaiah, J. R.; Gedam, R. S. Photocatalytic hydrogen production, dye degradation, and antimicrobial activity by Ag-Fe co-doped TiO_2 nanoparticles. *J. Mol. Liq.* **2023**, *369*, No. 120948.
(24) Slimani, Y.; Almessiere, M. A.; Mohamed, M. J. S.; Hannachi, E.; Caliskan, S.; Akhtar, S.; Baykal, A.; Gondal, M. A. Synthesis of Ce and Sm Co-Doped TiO_2 Nanoparticles with Enhanced Photocatalytic Activity for Rhodamine B Dye Degradation. *Catalysts* **2023**, *13* (4), 668.
(25) Yang, C.; Yi, C.; Liao, Q.; Li, N.; Zhao, Y. Ultrasonication-assisted synthesis of CN−TiO_2 and its photocatalytic degradation of diclofenac under visible light irradiation. *Environ. Technol.* **2023**, *44* (24), 3667−3675.
(26) Mohamad Idris, N. H.; Cheong, K. Y.; Smith, S. M.; Lee, H. L. C,N-Codoped TiO_2 Nanoparticles Immobilized on Floating Alginate Beads for Diazinon Removal under Solar Light Irradiation. *ACS Appl. Nano Mater.* **2024**, *7* (16), 18273−18286.
(27) Mohamad Idris, N. H.; Rajakumar, J.; Cheong, K. Y.; Kennedy, B. J.; Ohno, T.; Yamakata, A.; Lee, H. L. Titanium Dioxide/Polyvinyl Alcohol/Cork Nanocomposite: A Floating Photocatalyst for the Degradation of Methylene Blue under Irradiation of a Visible Light Source. *ACS Omega* **2021**, *6* (22), 14493−14503.
(28) Safeen, K.; Ullah, R.; Safeen, A.; Zulfiqar; Kabeer, M.; Khan, R.; Ullah, H.; Zaman, A.; Shafique Ahmad, K.; Ullah Shah, M. Z.; Elansary, H. O.; Mohamed Moussa, I.; Casini, R.; Mahmoud, E. A. Structure phase-dependent dielectric and photodegradation properties of Co-doped TiO_2 nanoparticles synthesized via co-precipitation route. *J. Saudi Chem. Soc.* **2023**, *27* (5), No. 101711.
(29) Abbad, S.; Guergouri, K.; Gazaout, S.; Djebabra, S.; Zertal, A.; Barille, R.; Zaabat, M. Effect of silver doping on the photocatalytic activity of TiO_2 nanopowders synthesized by the sol-gel route. *J. Environ. Chem. Eng.* **2020**, *8* (3), No. 103718.
(30) Jo, W.-K.; Kang, H.-J. Purification of BTEX at Indoor Air Levels Using Carbon and Nitrogen Co-Doped Titania under Different Conditions. *J. Environ. Sci.* **2012**, *21* (11), 1321−1331.
(31) Tze-Wei, B.; Abu Bakar, N. H. H.; Tan, W.; Abu Bakar, M.; Sabri, N.; Hussin, M. Properties of Natural Rubber: Magnetite Decorated with Silver Nanoparticles for Catalytic Degradation of Model Organic Contaminant. *J. Inorg. Organomet. Polym. Mater.* **2024**, *34*, 3511−3526.
(32) Chen, D.; Cheng, Y.; Zhou, N.; Chen, P.; Wang, Y.; Li, K.; Huo, S.; Cheng, P.; Peng, P.; Zhang, R.; Wang, L.; Liu, H.; Liu, Y.; Ruan, R. Photocatalytic degradation of organic pollutants using TiO_2-based photocatalysts: A review. *J. Cleaner Prod.* **2020**, *268*, No. 121725.
(33) Natarajan, T. S.; Mozhiarasi, V.; Tayade, R. J. Nitrogen Doped Titanium Dioxide (N-TiO_2): Synopsis of Synthesis Methodologies, Doping Mechanisms, Property Evaluation and Visible Light Photocatalytic Applications. *Photochem* **2021**, *1* (3), 371−410.
(34) Li, W.; Liang, R.; Zhou, N. Y.; Pan, Z. Carbon Black-Doped Anatase TiO_2 Nanorods for Solar Light-Induced Photocatalytic Degradation of Methylene Blue. *ACS Omega* **2020**, *5* (17), 10042−10051.
(35) Suriyachai, N.; Chuangchote, S.; Laosiripojana, N.; Champreda, V.; Sagawa, T. Synergistic effects of co-doping on photocatalytic activity of titanium dioxide on glucose conversion to value-added chemicals. *ACS Omega* **2020**, *5* (32), 20373−20381.
(36) Wang, J.; Wang, Y.; Wang, W.; Peng, T.; Liang, J.; Li, P.; Pan, D.; Fan, Q.; Wu, W. (2020). Visible light driven Ti^{3+} self-doped TiO_2 for adsorption-photocatalysis of aqueous U(VI). *Environ. Pollut.* **2020**, *262*, No. 114373.
(37) Rahman, S.; Nawaz, R.; Khan, J. A.; Ullah, H.; Irfan, M.; Glowacz, A.; Lyp-Wronska, K.; Wzorek, L.; Asif Khan, M. K.; Jalalah, M.; Alsaiari, M. A.; Almawgani, A. H. Synthesis and characterization of carbon and carbon-nitrogen doped black TiO_2 nanomaterials and their application in sonophotocatalytic remediation of treated agro-industrial wastewater. *Materials* **2021**, *14* (20), 6175.
(38) Bharti, B.; Kumar, S.; Lee, H.-N.; Kumar, R. Formation of oxygen vacancies and Ti^{3+} state in TiO_2 thin film and enhanced optical properties by air plasma treatment. *Sci. Rep.* **2016**, *6* (1), 32355.
(39) Piątkowska, A.; Janus, M.; Szymański, K.; Mozia, S. C-, N-and S-doped TiO_2 photocatalysts: A review. *Catalysts* **2021**, *11* (1), 144.
(40) Yang, Y.; Liao, S.; Shi, W.; Wu, Y.; Zhang, R.; Leng, S. Nitrogen-doped TiO_2(B) nanorods as high-performance anode materials for rechargeable sodium-ion batteries. *RSC Adv.* **2017**, *7* (18), 10885−10890.
(41) Thambiliyagodage, C.; Mirihana, S. Photocatalytic activity of Fe and Cu co-doped TiO_2 nanoparticles under visible light. *J. Sol-Gel Sci. Technol.* **2021**, *99* (1), 109−121.
(42) Chen, X.; Du, S.; Gao, L.; Shao, K.; Li, Z.; Liu, B. A hydrangea-like nitrogen-doped ZnO/BiOI nanocomposite for photocatalytic degradation of tetracycline hydrochloride. *Nanoscale Adv.* **2023**, *5* (7), 1936−1942.
(43) Waheed, A.; Baig, N.; Ullah, N.; Falath, W. Removal of hazardous dyes, toxic metal ions and organic pollutants from wastewater by using porous hyper-cross-linked polymeric materials: A review of recent advances. *J. Environ. Manage.* **2021**, *287*, No. 112360.
(44) Jasni, J.; Arisht, S. N.; Mohd Yasin, N. H.; Abdul, P. M.; Lin, S.-K.; Liu, C.-M.; Wu, S.-Y.; Jahim, J. M.; Takriff, M. S. Comparative

https://doi.org/10.1021/acsomega.4c08813
ACS Omega 2025, 10, 2858−2870

toxicity effect of organic and inorganic substances in palm oil mill effluent (POME) using native microalgae species. *J. Water Process Eng.* **2020**, *34*, No. 101165.
(45) Yang, J.; Chang, X.; Wei, F.; Lv, Z.; Liu, H.; Li, Z.; Wu, W.; Qian, L. High performance photocatalyst TiO_2@UiO-66 applied to degradation of methyl orange. *Discover Nano* **2023**, *18* (1), 112.
(46) Zainuri, N. Z.; Hairom, N. H. H.; Sidik, D. A. B.; Desa, A. L.; Misdan, N.; Yusof, N.; Mohammad, A. W. Palm oil mill secondary effluent (POMSE) treatment via photocatalysis process in presence of ZnO-PEG nanoparticles. *J. Water Process Eng.* **2018**, *26*, 10−16.
(47) Saputera, W. H.; Amri, A. F.; Daiyan, R.; Sasongko, D. Photocatalytic technology for palm oil mill effluent (POME) wastewater treatment: Current progress and future perspective. *Materials* **2021**, *14*, 2846.
(48) Meynen, V.; Cool, P.; Vansant, E. F. Verified syntheses of mesoporous materials. *Microporous Mesoporous Mater.* **2009**, *125* (3), 170−223.
(49) Yap, C.-T. J.; Lam, S.-M.; Sin, J.-C.; Zeng, H.; Li, H.; Huang, L.; Lin, H. Treatment of diluted palm oil mill effluent (POME) synchronous with electricity production in a persulfate oxidant-promoted photocatalytic fuel cell. *Environ. Sci. Pollut. Res.* **2023**, *30* (42), 96272−96289.
(50) Velmurugan, G.; Chohan, J. S.; Paramasivam, P.; Maranan, R.; Nagaraj, M. Green marvel: Harnessing spinach leaves' power for enhanced photodegradation of various effluents with biogenic ZnO nanoparticles. *Desalin. Water Treat.* **2024**, *319*, No. 100566.
(51) Putri, R. M.; Almunadya, N. S.; Amri, A. F.; Afnan, N. T.; Nurachman, Z.; Devianto, H.; Saputera, W. H. Structural Characterization of Polycrystalline Titania Nanoparticles on C. striata Biosilica for Photocatalytic POME Degradation. *ACS Omega* **2022**, *7* (48), 44047−44056.
(52) Charles, A.; Khan, M. R.; Ng, K. H.; Wu, T. Y.; Lim, J. W.; Wongsakulphasatch, S.; Witoon, T.; Cheng, C. K. Facile synthesis of $CaFe_2O_4$ for visible light driven treatment of polluting palm oil mill effluent: Photokinetic and scavenging study. *Sci. Total Environ.* **2019**, *661*, 522−530.
(53) Saputera, W. H.; Amri, A. F.; Mukti, R. R.; Suendo, V.; Devianto, H.; Sasongko, D. Photocatalytic Degradation of Palm Oil Mill Effluent (POME) Waste Using $BiVO_4$ Based Catalysts. *Molecules* **2021**, *26* (20), 6225.

https://doi.org/10.1021/acsomega.4c08813
ACS Omega 2025, 10, 2858−2870